







A High Spectral Resolution Study of the Soft X-Ray Background with the X-Ray Quantum Calorimeter

Dallas Wulf^{1,5} , Megan E Eckart^{2,6}, Massimiliano Galeazzi³, Felix Jaeckel¹, Richard L Kelley², Caroline A Kilbourne², Kelsey M Morgan^{1,7} , F Scott Porter², Dan McCammon¹ , and Andrew E Szymkowiak⁴ 

¹University of Wisconsin at Madison, Madison, WI 53706, USA; dallas.wulf@mcgill.ca

²NASA/Goddard Space Flight Center, Greenbelt, MD 20771, USA

³University of Miami, Coral Gables, FL 33146, USA

⁴Yale University, New Haven, CT 06520, USA

Received 2019 June 12; revised 2019 August 18; accepted 2019 September 4; published 2019 October 17

Abstract

We present here a combined analysis of four high spectral resolution observations of the Diffuse X-ray Background, made using the University of Wisconsin-Madison/Goddard Space Flight Center X-ray Quantum Calorimeter sounding rocket payload. The observed spectra support the existence of a ~ 0.1 keV Local Hot Bubble and a ~ 0.2 keV Hot Halo, with discrepancies between repeated observations compatible with expected contributions of time-variable emission from Solar Wind Charge Exchange. An additional component of ~ 0.9 keV emission observed only at low galactic latitudes can be consistently explained by unresolved dwarf M stars.

Key words: instrumentation: spectrographs – X-rays: diffuse background – X-rays: ISM

1. Introduction

Observations of diffuse X-rays below 1 keV revealed the presence of widely distributed hot gas in the Galaxy. We have come to realize that understanding the roles of this material in metal transport, stellar feedback, the disk–halo connection, and the exchange of matter with circumgalactic space is critical to central questions on the structure and evolution of galaxies. But useful observations for this purpose are difficult.

The Diffuse X-ray Background (DXRB) below 1 keV originates from several sources ranging from solar to extragalactic distance scales. With the exception of the Cosmic X-ray Background (CXRB), which can be represented by a power law, most of the DXRB flux in this energy range is in lines from highly charged ions. Hot interstellar gas at temperatures ranging from 1 to 4×10^6 K produces thermal emission throughout the Galaxy and Galactic halo. Closer to home, highly charged ions originating from the solar wind emit X-rays through an electron capture process known as charge exchange, or in this case specifically, Solar Wind Charge eXchange (SWCX; Cravens 1997; Koutroumpa et al. 2009; Galeazzi et al. 2014). These two very different emission mechanisms will produce the same lines, making them difficult to distinguish observationally. However, observations capable of resolving closely spaced lines in this part of the spectrum can utilize the relative intensity ratios of two or more lines from the same ion to constrain the relative contribution from each to the DXRB (see details in Section 5.1).

To date, very few observations of the DXRB have had the spectral resolution required to resolve individual emission lines.

All of the maps with broad sky coverage were made with gas proportional counters that have resolving powers, $R \equiv E/\Delta E$, of ~ 1 at 250 eV and ~ 2.5 at 1 keV. Slit-less grating spectrometers such as those on *Chandra* and *XMM-Newton* cannot be used on a very extended source such as the DXRB. Neither would adding slits help, because the surface brightness is too low to get an appreciable flux through a slit narrow enough to allow useful spectral resolution. Therefore, spectra must be obtained with energy-resolving detectors such as charge-coupled devices (CCDs) or microcalorimeters. Unfortunately, the statistics of charge formation fundamentally limit the resolving power of CCDs to ~ 15 at 600 eV. This is adequate to identify a few of the brightest lines between 500 and 1000 eV (e.g., O VII, O VIII, and Ne IX), but cannot resolve any of the more closely spaced lines below ~ 250 eV. Microcalorimeters get around the charge statistics limit by converting all of the photon energy to heat and measuring the temperature rise of the detector produced by a single photon.

Here we present a combined analysis of four high spectral resolution observations of the DXRB made by the University of Wisconsin-Madison/Goddard Space Flight Center sounding rocket payload, the X-ray Quantum Calorimeter (XQC). The XQC is a microcalorimeter X-ray spectrometer optimized for observing faint, extended sources like the DXRB below 1 keV with sufficient spectral resolution to identify individual emission lines. The paper proceeds as follows: details about the sounding rocket observations and hardware configurations are given in Section 2. In Sections 3 and 4, we describe the data reduction process and spectral analyses. A discussion of the inferred properties of the DXRB can be found in Section 5 and our conclusions in Section 6.

2. Sounding Rocket Observations

Table 1 summarizes the observing details of four XQC missions launched between 1999 and 2013. All missions were launched from White Sands Missile Range in New Mexico, USA (lat, long = 32:40:00N, 106:20:00W). The first two missions, 27.041 and 36.223, observed at high Galactic latitude

⁵ Current Address: McGill University, Montreal, QC H3A 2T8, Canada.

⁶ Current Address: Lawrence Livermore National Laboratory, Livermore, CA 94550, USA.

⁷ Current Address: National Institute of Standards and Technology, Boulder, CO 80305, USA.



Table 1
Summary of XQC Sounding Rocket Observations

Mission Number	Time (UT)	Date	Exposure (s)	Target (ℓ, b)
27.041	9:00	1999 Mar 28	100.7	$90^\circ, +60^\circ$
36.223	5:30	2008 May 1	176.9	$90^\circ, +60^\circ$
36.264	7:00	2011 Nov 5	205.4	$165^\circ, -5^\circ$
36.294	9:25	2013 Nov 3	150.0	$165^\circ, -5^\circ$

($\ell, b = 90^\circ, +60^\circ$), were chosen to be typical of high latitudes while avoiding the bright enhancements of Loop I and the North Polar Spur. The second two missions, 36.264 and 36.294, were observed at low Galactic latitude ($\ell, b = 165^\circ, -5^\circ$), avoiding emission associated with the Galactic center. Projections of the target areas onto all-sky maps are depicted in Figure 1. A previous analysis of the data from 27.041 was presented in McCammon et al. (2002), and data from 36.223 have been presented in Crowder et al. (2012). Data from 36.264 and 36.294 are presented here for the first time.

Mission 27.041 featured the first generation detector format described in McCammon et al. (2002), while the following three missions featured the larger detector format described in McCammon et al. (2008). Compared to the first detector, the new detector provides a factor of four improvement in collecting area (1.44 cm^2 compared to 0.36 cm^2), as well as improved energy resolution ($\sim 6 \text{ eV FWHM}$ below 1 keV compared to $\sim 9 \text{ eV FWHM}$). A hard landing destroyed the detector from Mission 36.223, but it was replaced by a similar detector for Missions 36.264 and 36.294. All four observations feature a $\sim 1 \text{ sr}$ non-imaging field of view, providing large throughput motivated by the low surface brightness of the DXRB. A minimum of five thin aluminized polyimide filters ranging in temperature from 0.05 to 130 K were used to shield the detector plane from 300 K infrared radiation ($\lambda \gtrsim 2 \mu\text{m}$) while still having acceptable transmission to soft X-rays. On the most recent flight, an outer sixth filter held at 300 K was added to prevent contamination of the inner cold filters. The issue of filter contamination is discussed more detail in Section 3.3. For a more detailed description of the payload, detector, and infrared-blocking filters, the reader is referred to McCammon et al. (2002, 2008).

3. Data Reduction

Due to a limited telemetry bandwidth, only triggered data segments containing X-ray events are telemetered to the ground station during an observation. Although almost 100% of X-ray events are contained within this data set, segments containing more than one event cannot be processed with optimum spectral resolution, effectively reducing detector livetime. Therefore, beginning with Mission 36.223, on-board flash storage was installed, enabling retrieval of complete time series data for all pixels upon payload recovery. The complete time series data permits the use of an overlapped pulse-fitting algorithm (Wulf et al. 2016, 2019), which is capable of processing these closely spaced X-ray events without loss of resolution. Missions 36.223, 36.264, and 36.394 were each reprocessed with the most recent version of this algorithm. No changes were made to the data reduction of 27.041 from McCammon et al. (2002).

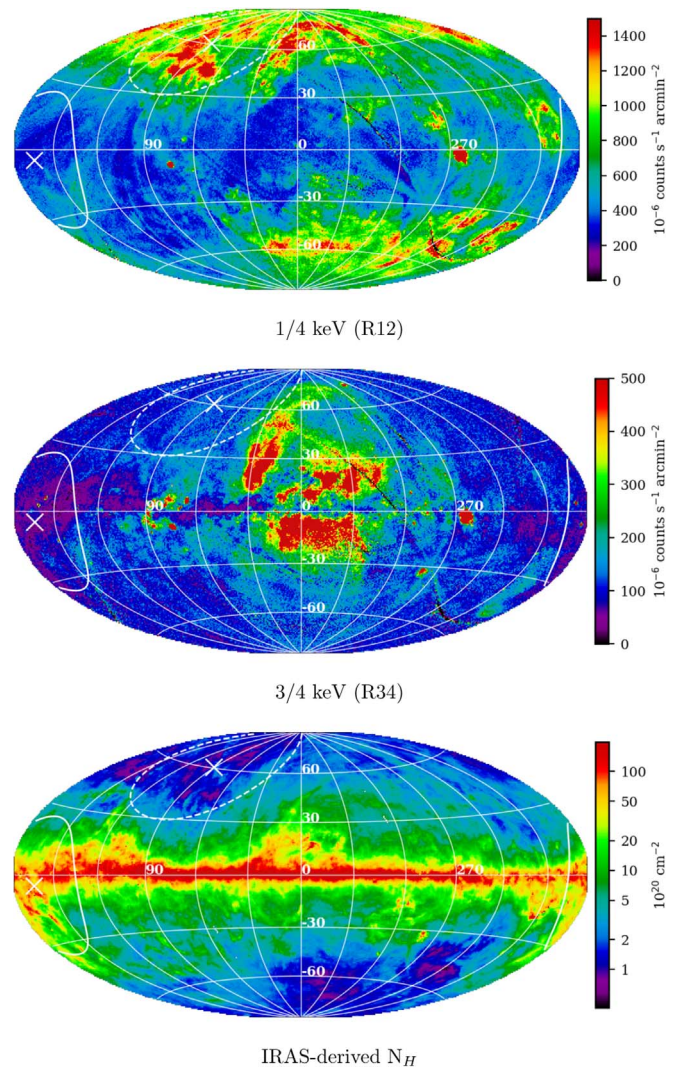


Figure 1. Target area of XQC observations projected on all-sky maps. Maps are in Galactic coordinates with the plane of the Galaxy located along the equator and the center of the Galaxy at the center of the map. The $\sim 1 \text{ sr}$ XQC fields of view are centered at $\ell, b = 90^\circ, +60^\circ$ (dashed line) and $\ell, b = 165^\circ, -5^\circ$ (solid line). *ROSAT* maps of R12 and R34 are from Snowden et al. (1997), and IRAS map is from data in Schlegel et al. (1998) converted to equivalent H I column.

3.1. Gain and Linearity Corrections

The gain of a microcalorimeter changes with temperature, partly because the heat capacity of the absorber increases with temperature, but primarily because the temperature response of the thermometers is nonlinear. While the coldplate temperature can generally be precisely regulated at 50 mK, changes in the thermal environment can affect the temperature offset between the pixels and the coldplate, and thus impact the gain. To track these gain changes, a ^{41}Ca calibration source continuously illuminates the entire array with $\text{K K}\alpha$ and $\text{K}\beta$ X-rays (3.31 and 3.59 keV, respectively).

The same nonlinear thermometer response, which is responsible for temperature dependent gain, is also responsible for a nonlinear energy response (i.e., as the temperature of the pixel changes during an X-ray event, the gain also changes). In order to convert measured pulse height to energy, a cubic polynomial is fit to calibration data containing emission lines of known energy. For this purpose, there is a multi-target fluorescent

calibration source installed on the inside of the gate-valve slide which emits a range of characteristic X-ray lines between 183 and 1740 eV, and which is visible to the detector whenever the gate-valve is closed. For each mission, calibration data for establishing the nonlinear energy scale were collected during ~ 30 minutes immediately preceding the launch.

3.2. Event Selection

The overlapped pulse-fitting algorithm is capable of processing nearly 100% of X-ray events. However, high energy events that cause saturation of the analog to digital conversion ($\gtrsim 10$ keV) cannot be analyzed, and are therefore excised from the data streams prior to processing. Any other X-ray events that are within the optimal filter length of a saturating event must also be removed. This must be done to ensure that the remaining events are all processed with optimum resolution. This cut dominates the processing deadtime for the three observations that are processed this way. Additionally, an event is excluded from the final analysis if it arrives within 10 ms following another event on the same pixel, and two events are excluded if they arrive within 2.5 ms of each other on adjacent pixels. The first condition removes events which are subject to rapidly changing gain due to the pixel cooling from the previous event. The second condition removes cosmic ray events and other sources of thermal cross-talk that deposit energy in neighboring pixels, resulting in events that are otherwise indistinguishable from true X-ray events. These event selection intervals can be compared with the 1.5 and 9 ms typical rise and fall times of the detectors, and they introduce negligible additional deadtime.

Finally, all the events from a single pixel are excluded if the arrival time distribution of events on that pixel is significantly different from a random distribution described by a single rate, or if the energy distribution (i.e., the spectrum) is significantly different than that of the entire detector array. The spectral comparison is made using the *K*-Sample Anderson–Darling test for equality (Scholz & Stephens 1987), chosen because it is non-parametric (i.e., requires no assumptions about the underlying data distribution), and has sensitivity at the tails of the distribution. Pixels were considered to fail this test if the null hypothesis was rejected at the 95% level. These tests are an added safeguard to ensure that time- and pixel-dependent gain corrections do not introduce any distortions to the final spectrum. Depending on the observation, these tests affected between three and five pixels.

3.3. Filter Contamination

Beginning with Mission 36.223, water ice contamination to the infrared-blocking filters became an issue. Calibration data from immediately before and after the observation confirmed that the contamination formed during the time that the gate-valve was open, suggesting that the source of the contamination was outside the cryostat. Between Missions 27.041 and 36.223, a hermetic bulkhead was removed between the experiment section and the other sections of the payload. The source of the contamination was initially assumed to be the payload venting through the experiment section. For Mission 36.264 therefore, the payload was purged with dry nitrogen gas prior to launch. Unfortunately, this remedy failed to prevent water ice from accumulating on the filters, with total ice accumulation actually being worse than the previous mission. For Mission 36.294, a sixth outermost filter held at 300 K was added. While the

additional filter reduced throughput slightly, it successfully prevented ice from forming on the filters, resulting in a net improvement to throughput. The exact source of water vapor responsible for the ice is still unknown.

For Missions 36.223 and 36.264, the correction for contaminated filter transmission is based on a combination of post-flight data (taken on the parachute after re-entry into the atmosphere) and in-flight data. The same gate-valve calibration source described in Section 3.1 used to establish the nonlinear gain scale prior to flight also provides a relative measurement of filter transmission following the observation. These data have the advantage of measuring the transmission at well-defined energies, but sample a relatively small fraction of the filter area and only provide an estimate of the total ice accumulated at the end of the observation. To complement this measurement, the on-sky spectrum measured throughout the observation is compared to predictions made by the *ROSAT* All-sky Survey (RASS) data. In contrast to the gate-valve data, these data sample the entire filter area and provide time-domain information about ice accumulation, though measure only the RASS band-averaged transmission. For both flights affected by ice contamination, self-consistent models for filter transmission are selected using both of these measurements.

3.4. Non X-Ray Background

The primary source of background events in the 100–1100 eV range is higher energy X-rays that have lost energy due to photoelectric escape. Whenever an X-ray is stopped near the surface of the pixel, there is some probability that it will eject an electron from the surface via the photoelectric effect. This happens $\sim 5\%$ of the time. The energy carried away by the electron is lost, resulting in a lower observed energy. The resulting spectrum can be approximated as flat between zero and the incident X-ray energy. For all four XQC observations, the internal ^{41}Ca calibration source at 3.3 and 3.7 keV is responsible for most of this background, contributing $0.5 \text{ counts s}^{-1} \text{ keV}^{-1}$ to the 36.223 spectrum and $0.3 \text{ counts s}^{-1} \text{ keV}^{-1}$ to the other three spectra (the calibration source intensity was greater for 36.223).

We also consider possible particle sources of backgrounds. For primary cosmic ray protons, the minimum ionizing energy loss in a pixel is $\gtrsim 5.5$ keV, and thus does not contribute to the low-energy spectrum directly. However, cosmic rays can also eject electrons from surfaces surrounding the detector array, which can produce events at lower energies. We have looked for evidence of background from such cosmic ray secondaries when the gate-valve is closed, but the observed spectrum has always been consistent with the spectrum taken with the gate-valve closed at sea level, suggesting that this background is negligible.

Another possible source of low energy particle background is auroral electrons. This has always been a concern for XQC, whose wide field of view prevents the use of magnetic brooms to keep electrons from entering the detector. Fortunately, with the exception of Mission 36.294, the data do not support a significant contribution from an electron background. This determination is made based on comparisons with the *ROSAT* survey data, which provide an approximate shape of the DXRB spectrum. Only for Mission 36.294 do we observe an excess flux of approximately $0.4 \text{ counts s}^{-1} \text{ keV}^{-1}$ in each of the *ROSAT* energy bands (~ 100 – 2500 eV). Auroral electrons provide a natural explanation for such a flat excess, as the energy loss through the infrared-blocking filters (~ 3 keV, depending on energy) serves to flatten almost any initial energy distribution.

Table 2
Observed Flux for all Four Missions Relative to the RASS Energy Bands

Mission	Relative <i>ROSAT</i> Band Flux (%)					
	R1	R2	R4	R5	R6	R7
27.041 ^a	...	143 ± 12	94 ± 7	81 ± 6	69 ± 6	89 ± 11
36.223	...	85 ± 14	97 ± 7	91 ± 5	99 ± 5	107 ± 7
36.264	...	65 ± 16	76 ± 10	81 ± 7	99 ± 7	106 ± 7
36.294	...	75 ± 9	92 ± 7	92 ± 6	109 ± 8	117 ± 10
Energy ^b (eV)	110–284	140–284	440–1010	560–1210	730–1560	1050–2040

Notes. R1 is not included due to large statistical uncertainties. Statistical uncertainties are given at the 1σ level.

^a Values from McCammon et al. (2002).

^b 10% of peak response (Snowden et al. 1997).

3.5. Cross Check

As a consistency check on the absolute flux, the final event selection is compared to the band fluxes measured by the RASS. The energy resolution of XQC allows us to make a model-independent comparison by simply multiplying the observed spectra by the ratio of the *ROSAT* Position Sensitive Proportional Counter (PSPC) response to the XQC response at the energy observed by XQC. The relative fluxes and band energies are listed in Table 2. The reader is referred to Snowden et al. (1997) for a complete description of the *ROSAT* PSPC broad energy bands. For the three most recent missions, we find good agreement with the *ROSAT* data, especially at higher energies. Notably, we find the largest discrepancy in the R2 band for all observations. As will be discussed later in Section 5, this discrepancy can be explained by variability in the contribution from heliospheric SWCX. For Mission 36.264, there is also a discrepancy observed in the R4 and R5 bands, though this is also the mission with the most significant filter contamination from water ice. As bands R4 and R5 are situated above the oxygen *K*-edge, they are especially sensitive to the temporal and spatial distributions of ice accumulation, which may not be captured by the model for ice transmission. Relative fluxes for Mission 27.041 have been previously reported in McCammon et al. (2002).

4. Spectral Analysis

Spectral fitting was performed with XSPEC version 12.9.0, using the PyXspec interface (Arnaud 1996). Thermal emission was modeled with APEC version 2.0.2 (Smith et al. 2001) using solar abundances from Anders & Grevesse (1989). Depleted abundances from Savage & Sembach (1996) were also considered, but were not found to improve the fits. Charge exchange emission was modeled with AtomDB’s Charge eXchange model, VACX, version 1.0.1 (Smith et al. 2012). Following Smith et al. (2014), two SWCX components representing contributions from fast and slow solar wind were used, with relative abundances taken from Table 1 in von Steiger et al. (2000).

Interstellar absorption of the CXRB and hot Galactic halo was calculated from the transmission-weighted average over the full XQC field of view. The column depth of the Galaxy in each direction was derived from the Infrared Astronomical Satellite (IRAS) 100 μm map, calibrated by the Diffuse Infrared Background Experiment onboard the Cosmic Background Explorer satellite (Schlegel et al. 1998). This infrared emission map is intended to approximate dust mass, which we can convert to

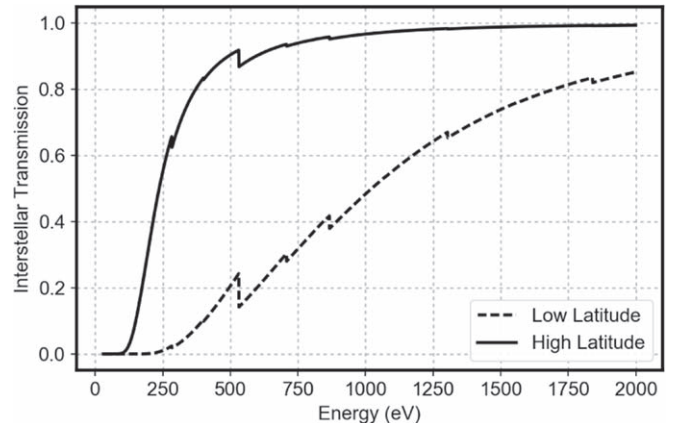


Figure 2. Interstellar transmission averaged over XQC fields of view. This transmission is used to account for interstellar absorption of the Cosmic X-ray Background (CXRB) and hot Galactic halo emission in spectral models.

total hydrogen column depth by assuming an average gas-to-dust ratio. The equivalent hydrogen column depth is obtained by multiplying by a factor of $1.44 \times 10^{20} \text{ cm}^{-2} \text{ MJy}^{-1}$, as outlined in Snowden et al. (1997). This approach is favored over other tracers of hydrogen column depth (e.g., 21 cm emission) as it accounts for both atomic and molecular gas—the latter of which can contribute significantly at low galactic latitudes. Transmission was calculated assuming solar abundances from Anders & Ebihara (1982) and cross sections from Balucinska-Church & McCammon (1992). The resulting average interstellar transmission for each target area is shown in Figure 2.

All four spectra were fit with a minimum of four model components: (1) an unabsorbed APEC plasma representing emission from the Local Hot Bubble (LHB); (2) an unabsorbed VACX component representing SWCX due to slow solar wind; (3) an absorbed APEC plasma representing emission from the hot Galactic halo; and (4) an absorbed double broken power law representing the CXRB due to unresolved extragalactic active galactic nuclei. For the low latitude observations, an additional absorbed power-law component was included to represent the Crab Nebula, which was within the field of view. The low latitude observations also required an additional thermal component at $\sim 0.9 \text{ keV}$, interpreted as a contribution from dwarf M (dM) stars and modeled by an absorbed, two temperature APEC plasma. Further details of this model and its motivations are presented in Section 5.4. Lastly, the spectrum from Mission 27.041 required an additional unabsorbed VACX

Table 3
Model Parameters for Simultaneous fit of High-latitude Observation

Component	Model	Parameter	Value	
			27.041	36.223
Local Hot	APEC ^a	kT (keV)	$0.093^{+0.010}_{-0.019}$	
Bubble		Normalization ^b	$8.09^{+1.92}_{-1.79}$	
Fast SWCX	VACX ^c	kT (keV)	$0.055^{+0.011}_{-0.006}$	
		Normalization ^d	$4.17^{+3.54}_{-2.25}$	
Slow SWCX	VACX ^c	kT (keV)	$0.184^{+0.042}_{-0.045}$	
		Normalization ^d	$0.073^{+0.059}_{-0.042}$	$0.023^{+0.019}_{-0.016}$
Hot Halo	Absorbed	kT (keV)	$0.189^{+0.026}_{-0.018}$	
	APEC ^{a,c}	Normalization ^b	$4.99^{+2.04}_{-1.75}$	
CXRB	Absorbed Double Broken Power Law ^{e,f}	Photon Index 1	1.54	
		Normalization 1 ^g	5.7	
		Photon Index 2 ($E < E_{\text{break}}$)	1.96	
		Normalization 2 ^g	4.9	
		E_{break} (keV)	1.2	
		Photon Index ($E > E_{\text{break}}$)	1.4	
		χ^2/dof^h	997.67/788 = 1.266	

Note. All uncertainties are reported at 90% confidence level. In instances where a component or parameter is unique to a single spectrum, the values are reported in the column of the corresponding spectrum.

^a Solar abundances from Anders & Grevesse (1989).

^b Units of $10^{14} \text{ cm}^{-5} \text{ sr}^{-1}$.

^c Relative abundances from Table 1 in von Steiger et al. (2000).

^d Parameter has no intrinsic physical unit. See text for discussion.

^e Transmission-weighted average interstellar absorption (Figure 2).

^f Double power-law model given by Smith et al. (2007).

^g Units of photons $\text{keV}^{-1} \text{ s}^{-1} \text{ cm}^{-2} \text{ sr}^{-1}$ at 1 keV.

^h Pearson's χ^2 statistic (Pearson 1900).

charge exchange component representing SWCX due to fast solar wind. This component differs from the slow solar wind primarily in its ion temperature, but also differs slightly in elemental abundances.

A summary of model components and parameters are listed in Tables 3 and 4. Repeat observations of the same target were fit simultaneously with common model parameters, with the exception of the SWCX components, which have free normalizations for each observation. Parameters for the CXRB and Crab were not fit, and instead were fixed to values from the literature. Figures 3–6 show each of the four spectra and corresponding models folded through the instrumental response, and individual model components are depicted in Figures 7 and 8.

5. Discussion

5.1. Solar Wind Charge Exchange

The VACX model used to generate SWCX spectra is only approximate, since it lacks any dependence on the solar wind velocity. Laboratory measurements of charge exchange emission spectra have demonstrated that the relative strength of different emission lines changes significantly over the range of solar wind

Table 4
Same as Table 3 Except for Low Latitude Observations

Component	Model	Parameter	Value	
			36.264	36.294
Local Hot	APEC	kT (keV)	0.099 (fixed)	
Bubble		Normalization	$3.15^{+0.72}_{-0.69}$	
Slow SWCX	VACX	kT_C (keV)	$0.088^{+0.011}_{-0.020}$	
		kT (keV)	$0.176^{+0.016}_{-0.020}$	
		Normalization	$0.047^{+0.028}_{-0.023}$	$0.069^{+0.033}_{-0.027}$
Hot Halo	Absorbed	kT (keV)	$0.245^{+0.069}_{-0.059}$	
	APEC	Normalization	$4.92^{+4.28}_{-3.08}$	
dM Stars	Absorbed	Normalization ^a	$1.00^{+0.27}_{-0.26}$	
CXRB	Absorbed Double Broken Power Law	Photon Index 1	1.54	
		Normalization 1	5.7	
		Photon Index 2 ($E < E_{\text{break}}$)	1.96	
		Normalization 2	4.9	
		E_{break} (keV)	1.2	
		Photon Index ($E > E_{\text{break}}$)	1.4	
		χ^2/dof	1096.66/788 = 1.392	

Notes.

^a Dimensionless. See text for description of model and normalization parameter.

^b Absorbed power law given by Table 1 in Weisskopf et al. (2010).

^c Units of photons $\text{keV}^{-1} \text{ s}^{-1} \text{ cm}^{-2}$ at 1 keV.

velocities (e.g., Defay et al. 2013). There are also large uncertainties and variabilities in the metal ion content of the solar wind. Nevertheless, the two SWCX components used here improve the fits and help resolve differences between repeat observations of the same target—especially at high latitudes. With the exception of Mission 27.041, the relative contribution tends to be less than estimates for heliospheric SWCX in the RASS R12 maps (Table 5). This difference is likely responsible for the discrepancy in Table 2 at low energies. As previously mentioned, 27.041 is the only observation to require a significant contribution from fast solar wind. For the simultaneous fit to the high-latitude observations, the addition of the fast solar wind component to the 27.041 spectral model improves the goodness of fit by $\Delta\chi^2/\Delta\text{dof} = 83.99/2$. Coincidentally, this is also the only observation to exhibit strong excess emission at 263 eV (See Figure 3). Perhaps this feature may be attributed to L-shell emission from solar wind ions S IX or Si X, but which is not included in this single temperature model for the fast solar wind.

A more robust measurement of the SWCX contribution can be made by analyzing individual emission lines, made possible by the high spectral resolution of these observations. After fitting a global model to each spectrum, the intensities of

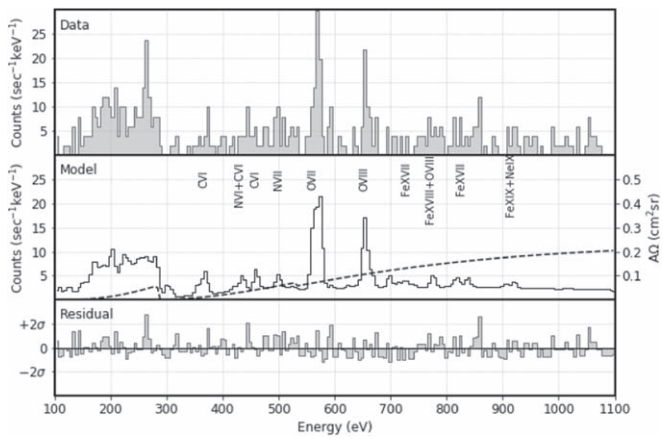


Figure 3. 27.041 high-latitude spectrum. Data are shown in the top panel with the model from Table 3 shown in the middle panel. The dashed line represents the energy-dependent effective area. Residuals are shown in the bottom panel in units of sigma, estimated from the model. All histograms have 5 eV bins.

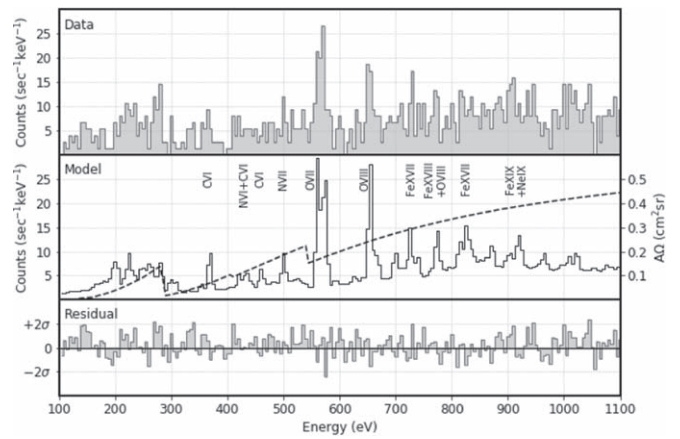


Figure 6. 36.294 low latitude spectrum. Data are shown in the top panel with the model from Table 4 shown in the middle panel. The dashed line represents the energy-dependent effective area. Residuals are shown in the bottom panel in units of sigma, estimated from the model. All histograms have 5 eV bins.

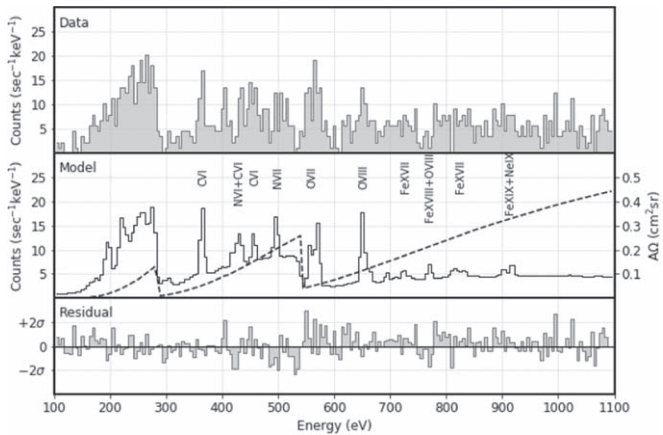


Figure 4. 36.223 high-latitude spectrum. Data are shown in the top panel with the model from Table 3 shown in the middle panel. The dashed line represents the energy-dependent effective area. Residuals are shown in the bottom panel in units of sigma, estimated from the model. All histograms have 5 eV bins.

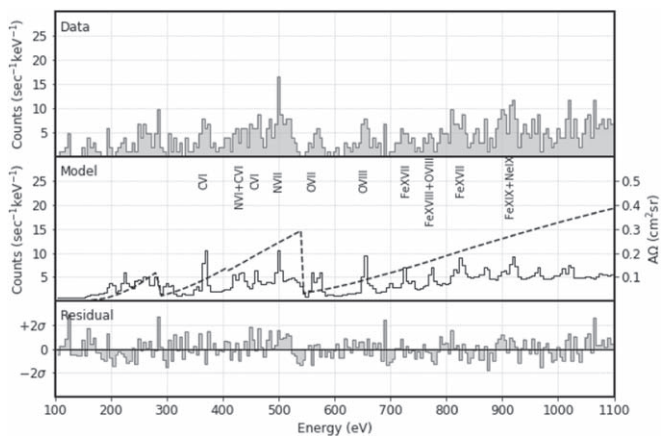
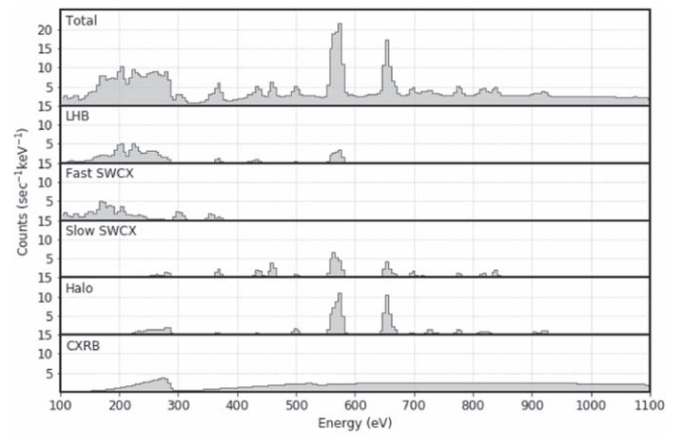
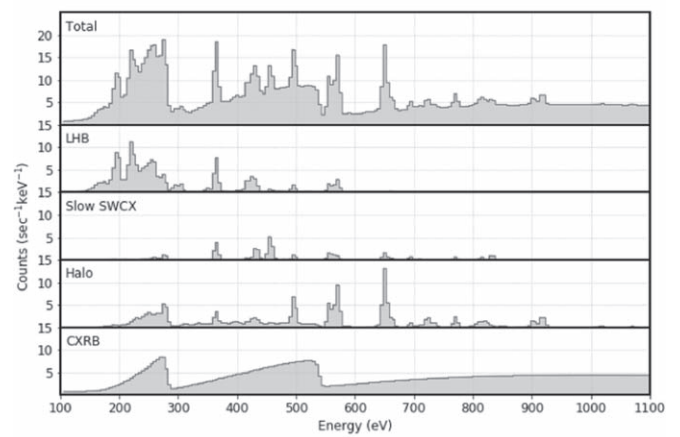


Figure 5. 36.264 low latitude spectrum. Data is shown in the top panel with the model from Table 4 shown in the middle panel. The dashed line represents the energy-dependent effective area. Residuals are shown in the bottom panel in units of sigma, estimated from the model. All histograms have 5 eV bins.

individual lines are measured by setting the abundance for a single element to zero in each of the model components and adding δ -functions for each of the strong lines of that element.



27.041



36.223

Figure 7. High-latitude model components (Table 3). Non X-ray background is negligible in all cases.

Fluxes measured in this manner for select emission lines are presented in Table 6, with ratios of those lines given in Table 7. Of particular interest are lines from C VI and O VII, since they are relatively bright, are isolated from other lines, and can be used to unambiguously differentiate between thermal emission and SWCX.

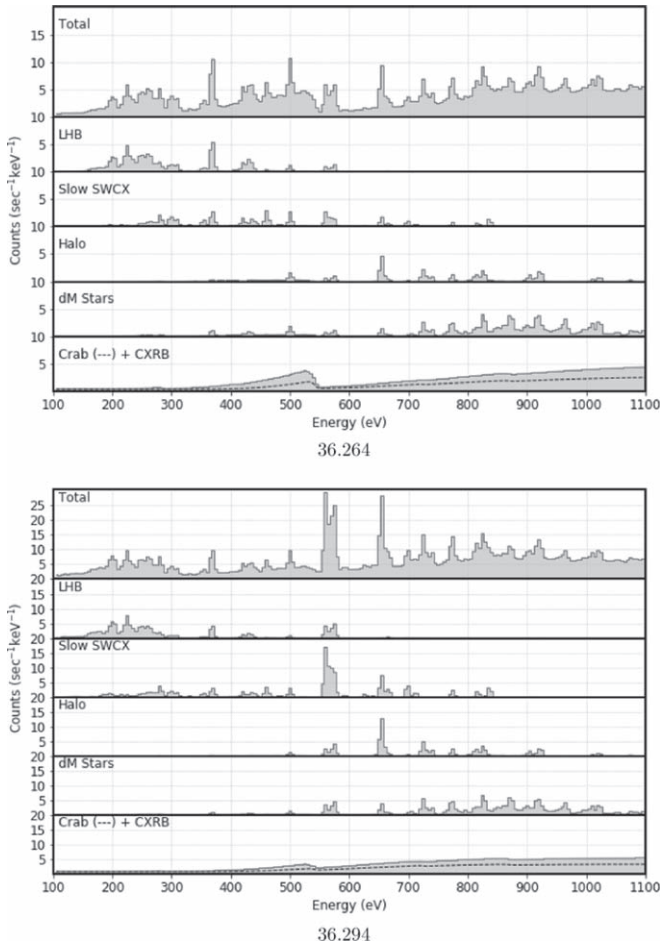


Figure 8. Low latitude model components (Table 4). Non X-ray background is negligible in all cases.

Table 5

Combined Contribution of Fast and Slow SWCX Model Components in Tables 3 and 4 to the *ROSAT* Energy Bands R1 and R2, Compared to Estimates for the RASS R1 and R2 Maps given by Uprety et al. (2016)

Target	Mission	SWCX Flux (RU ^a)	
		R1	R2
High Latitude	27.041	489 ⁺⁴¹⁴ ₋₂₆₅	234 ⁺¹⁹⁷ ₋₁₂₇
	36.223	22 ⁺¹⁹ ₋₁₆	12 ⁺¹¹ ₋₉
	RASS	70	110
Low Latitude	36.264	22 ⁺¹³ ₋₁₁	18 ⁺¹⁰ ₋₉
	36.294	28 ⁺¹³ ₋₁₁	25 ⁺¹² ₋₁₀
	RASS	55	81

Note. All uncertainties are reported at 90% confidence level.

^a 1 RU $\equiv 10^{-6}$ counts s^{-1} arcmin⁻².

As noted by a previous analysis of Mission 36.223, the $Ly\gamma/Ly\alpha$ ratio of H-like C VI and the G -ratio of He-like O VII can be used to constrain the allowed thermal contribution to the observed emission from these respective ions (Crowder et al. 2012). Although the ratios for SWCX spectra depend on both collision velocity and electron donor (e.g., hydrogen versus helium), upper limits can be used to conservatively estimate the minimum possible contribution from SWCX (Greenwood et al. 2001; Koutroumpa 2007; Defay et al. 2013; Fogle et al. 2014).

Table 6
Line Identification and Fluxes

Emission Line	Energy (eV)	Flux (LU ^a)			
		27.041	36.223	36.264	36.294
C VI Ly α	368	5.88 ^{+5.15} _{-3.55}	2.02 ^{+1.03} _{-0.84}	0.77 ^{+0.46} _{-0.36}	0.86 ^{+0.68} _{-0.49}
C VI Ly- γ	459	<2.02	0.38 ^{+0.37} _{-0.29}	0.24 ^{+0.21} _{-0.16}	<0.36
O VII $K\text{-}\alpha$ F	561	...	1.88 ^{+1.20} _{-0.93}	0.69 ^{+0.82} _{-0.58}	1.12 ^{+0.48} _{-0.40}
O VII $K\text{-}\alpha$ I	569	...	<2.07	<1.37	0.59 ^{+0.49} _{-0.41}
O VII $K\text{-}\alpha$ R	575	...	2.37 ^{+1.18} _{-0.96}	0.59 ^{+0.75} _{-0.50}	0.62 ^{+0.44} _{-0.35}
O VIII Ly α	654	1.48 ^{+0.79} _{-0.61}	0.91 ^{+0.48} _{-0.39}	0.74 ^{+0.47} _{-0.35}	0.69 ^{+0.31} _{-0.25}

Notes. F, I, and R refer to the forbidden, intercombination, and resonance lines due to the fine structure splitting of the He-like $K\text{-}\alpha$ triplet. The O VII $K\text{-}\alpha$ fine structure splitting could not be resolved for mission 27.041, though a total flux of $4.74^{+1.52}_{-1.41}$ LU is observed for the triplet. All uncertainties and limits are reported at 90% confidence level.

^a 1 LU $\equiv 1$ photon s^{-1} cm^{-2} sr^{-1}

For an observed line ratio R_{obs} and predicted ratios for thermal and SWCX emission, R_{therm} and R_{swcx} , the inferred fraction due to thermal emission, F_{therm} , is given by Equation (1).

$$F_{\text{therm}} = \frac{(1 + R_{\text{therm}})(R_{\text{swcx}} - R_{\text{obs}})}{(1 + R_{\text{swcx}})(R_{\text{swcx}} - R_{\text{therm}})}. \quad (1)$$

Table 8 presents the results of this analysis. In agreement with the previous analysis, we find that thermal emission likely dominates the observed emission for both C VI and O VII at high latitudes, though the statistical uncertainties allow for a non-negligible contribution from SWCX.

At low latitudes we find that SWCX is likely responsible for at least half of the observed O VII emission, though this seems to be due to a reduction in thermal emission compared to the high-latitude observations, rather than an increase in SWCX. At all latitudes, we find that SWCX accounts for ~ 1 LU (1 LU $\equiv 1$ photon s^{-1} cm^{-2} sr^{-1}) of O VII $K\alpha$ emission. SWCX may also be dominating C VI emission in the Mission 36.264 observation, though this not statistically very significant. Initial fits to the low latitude spectra using the VACX model failed to predict the strong relative observed contribution to O VII. In order to reproduce the O VII flux inferred from the G -ratio, the ion temperature of carbon in the VACX model (kT_C in Table 4) was allowed to vary independently of the temperature of the other ions.

Archival data available through OMNIWeb⁸ was used to get solar wind proton fluxes during each observation, time-shifted to Earth. The fluxes are $< 3 \times 10^8$ cm^{-2} s^{-1} during each observation, which is below the level that Yoshino et al. (2009) finds to be associated with significant contributions from geocoronal SWCX in Suzaku observations. Moreover, the near midnight zenith viewing geometry of sounding rocket observations makes them less susceptible to contamination from geocoronal SWCX, which originates most strongly from the Earth's subsolar magnetosheath (Robertson & Cravens 2003). For these reasons, it is more likely that SWCX emission observed here is of heliospheric origin.

5.2. Hot Galactic Halo

A single temperature halo model was used for this analysis, with a best-fit temperature of ~ 0.2 keV at both low and high

⁸ <http://omniweb.gsfc.nasa.gov/>

Table 7
Ratios of Lines Identified in Table 6

Ratio	27.041	36.223	36.264	36.294	Thermal Prediction ^a	SWCX Prediction ^b
C VI Ly- γ /Ly α	0.13 \pm 0.09	0.19 \pm 0.07	0.31 \pm 0.13	0.10 \pm 0.08	0.04	0.5
O VII (F+I)/R ^c	...	1.19 \pm 0.33	2.03 \pm 1.07	2.76 \pm 0.79	0.97	6.0

Notes. Statistical uncertainties estimated from the model are given at the 1σ level.

^a Based on APEC components in spectral model.

^b Line ratios for SWCX depend on both velocity and electron donor. Reported values are upper limits to conservatively estimate minimum possible SWCX contribution.

^c Also known as the *G*-ratio.

Table 8

Relative Thermal Contribution to Observed Emission Lines from Select Ions, Derived from Line Ratios given in Table 7 using Equation (1)

Ion	Thermal Fraction			
	27.041	36.223	36.264	36.294
C VI	0.75 ^{+0.25} _{-0.21}	0.59 ^{+0.18} _{-0.16}	0.33 ^{+0.29} _{-0.23}	0.81 ^{+0.19} _{-0.21}
O VII	...	0.86 ^{+0.14} _{-0.17}	0.51 ^{+0.49} _{-0.24}	0.34 ^{+0.20} _{-0.13}

Note. Statistical uncertainties estimated from the model are given at the 1σ level.

latitudes, assuming solar abundances. This is consistent with other observations that fit single temperature halos with $kT \sim 0.2$ keV (Yoshino et al. 2009). However, previous observations have also established that the thermal and spatial distribution of the halo is complex (e.g., Kuntz & Snowden 2000; Lei et al. 2009; Yao et al. 2009; Liu et al. 2016), and a single temperature model is therefore likely overly simplistic. One should be careful not to ascribe too much significance to any physical interpretation.

There is good evidence from cloud shadowing, small-scale absorption studies, and observations at lower energies that bright patches of ~ 0.1 keV emission in the Galactic halo contribute substantially to our high-latitude observations (Burrows & Mendenhall 1991, 1993; Snowden et al. 1998; Kuntz & Snowden 2000; Bellm & Vaillancourt 2005). However, an attempt to add an additional low-temperature component to our model resulted in no improvement to the fit. This is not surprising, given that these observations lack the spatial resolution used by other analyses to separate this component from the local plasma at approximately the same temperature. Therefore our LHB fluxes necessarily include this low-temperature halo contribution, as will be discussed further in Section 5.3.

5.3. The Local Hot Bubble

At both high and low latitudes, we fit a local plasma temperature of ~ 0.1 keV, using solar abundances. For reference, Snowden et al. (1998) reports 0.10 keV from an analysis of the RASS data. More recently, Liu et al. (2017) reanalyzed the RASS data taking contributions from SWCX into account and reports a temperature of 0.097 keV. Smith et al. (2014) modeled SWCX contributions to the DXS hot interstellar medium spectrum (Sanders et al. 2001) with the same VACX model used for this analysis and reports an LHB temperature of 0.097 keV with depleted abundances.

With the exception of the DXS observation, the data presented here have significantly better energy resolution than previous observations. Moreover, the aforementioned analyses

Table 9

Comparison of Local and Distant Contributions to *ROSAT* R12 band Fluxes After Correcting for Contribution from SWCX

Target	Instrument	Astrophysical R12 Flux (RU)		
		Local	Distant	Total
High Latitude	XQC	495 \pm 85	380 \pm 72	827 \pm 89
	RASS	383	448	831
Low Latitude	XQC	228 \pm 44	47 \pm 36	272 \pm 46
	RASS	247	17	264

Note. SWCX-corrected values for the RASS given by Liu et al. (2017). Statistical uncertainties estimated from the model are given at the 1σ level.

rely primarily on data below the carbon edge at 282 eV. Observations that include higher energy data including O VII $K\alpha$ emission at ~ 570 eV tend to fit higher temperatures that are inconsistent with lower energy observations, e.g., Yoshino et al. (2009). For the observations analyzed here, we find that the fit temperature of the LHB is very sensitive to the intensity of O VII. If included in the fit, we derive a low latitude LHB temperature that is inconsistent with the high-latitude observations. However, if the energy range is restricted to < 500 eV during the fit, then the 90% confidence temperature ranges agree at both latitudes (See Tables 3 and 4). As mentioned in Section 5.1, O VII is likely dominated by SWCX at low latitudes and this contribution is difficult to estimate with sufficient accuracy. Therefore, in this analysis the LHB temperature at low latitudes is fixed to the value derived from the low-energy spectrum before fitting the entire 100–1100 eV range.

As mentioned in Section 5.2, at high latitudes we are unable to separate the local plasma from the low-temperature component of the halo, which affects our derived values for emission measure, as well as possibly temperature. Liu et al. (2017) combined SWCX maps from Uprety et al. (2016) with data from Snowden et al. (1998) to estimate the local and distant astrophysical contributions to the R12 band. In Table 9, we compare the results of our spectral model fits to that work. At low latitudes, where the distant R12 emission is strongly absorbed, we find good agreement. At high latitudes, however, we overestimate the ratio of local to distant flux as we would expect without a low-temperature halo component. Nevertheless, at both latitudes our total derived flux from astrophysical sources is remarkably consistent with Liu et al. (2017). This provides a strong indication that the discrepancies seen at low energies in Table 2 do indeed arise from differences in heliospheric SWCX contribution.

Table 10

Spatial Density Distribution Parameters used in Spectral Emission Model for Combined Early- and Late-type dM Stars

Age (Gyr)	K_+ ^a (pc)	K_- ^a (pc)	c ^{a,b}	Midplane EM Density ^c ($10^{14} \text{ cm}^{-5} \text{ sr}^{-1} \text{ kpc}^{-1}$)
0–0.15	5000	3000	0.0140	2.93
0.15–1	2226	494.4	0.0279	0.85
1–2	2226	494.4	0.0457	0.07
2–3	2226	494.4	0.0662	0.05
3–5	2226	494.4	0.0867	0.07
5–10	2226	494.4	0.0958	0.16
Total				4.13

Notes.^a Scale parameters for (1) and (2) of Appendix A in Bienayme et al. (1987).^b Dimensionless ellipticity from Notes of Table 2 in Kuntz & Snowden (2001).^c Adapted from Table 2 in Kuntz & Snowden (2001) and Table 3 in Masui et al. (2009).

5.4. Stellar Contribution

At low latitudes, we observe excess emission around 0.9 keV arising from lines of Ne IX and Fe XVII–XIX, which suggests the existence of an additional thermal component of higher temperature than those previously discussed. While evidence of 0.7–1 keV diffuse gas has been observed in outflows toward the Galactic center (e.g., Ponti et al. 2019) and in the direction of the North Polar Spur (Das et al. 2019), it is difficult to confine a diffuse source of this temperature to low Galactic latitudes. Therefore, we investigated stars as a possible source of the emission, which have long been proposed to explain the excess 3/4 keV flux throughout the Galactic plane (e.g., Rosner et al. 1981; Kuntz & Snowden 2001; Gupta & Galeazzi 2009; Masui et al. 2009). Following Kuntz & Snowden (2001) and Masui et al. (2009), we constructed a spectral emission model of dwarf M stars (dM stars), taking into account Galactic absorption and spatial star distribution. Stellar spectra were approximated as a two temperature plasma with $T_C = 0.138 \text{ keV}$ and $T_H = 0.78 \text{ keV}$, based on *ROSAT* observations of nearby dM stars (Giampapa et al. 1996). Parameters detailing the spatial emission measure distribution of each temperature component are given in Table 10, normalized to $4.13 \times 10^{14} \text{ cm}^{-5} \text{ sr}^{-1} \text{ kpc}^{-1}$ in the plane of the Galaxy at the solar radius. Absorption was calculated from Equations (1) and (2) in Ferrière (2001). We then fit low latitude observations with this stellar model scaled by a single free normalization parameter. The best-fit value of this parameter is consistent with unity ($1.00_{-0.26}^{+0.27}$, see Table 4), providing quantitative agreement between the observed excess flux and model prediction. Moreover, the addition of this component provides a significant improvement to the goodness of fit ($\Delta\chi^2/\Delta\text{dof} = 103.7/1$). Since the scale height of the young (<0.15 Gyr) dM stars responsible for 71% of the X-ray emission in our model is even smaller than the gas scale height, the stellar X-ray contribution is expected to drop sharply with increasing Galactic latitude. Trying to fit this model to our high-latitude observations indicates an even steeper drop-off, with a 2σ upper limit of 1.05 for the normalization.

6. Conclusions

Here we presented a combined analysis of the past four XQC sounding rocket observations. The three most recent observations have all been processed with an overlapped pulse-fitting

algorithm to improve spectral resolution and reduce processing deadtime compared to conventional processing techniques. The resulting spectra are consistent with fluxes measured by the RASS, with discrepancies reasonably accounted for by the estimated contributions from SWCX. Likewise, repeated XQC observations of the same targets can be fit with identical spectral emission models, adjusting for differences in instrumental response and allowing for variable SWCX intensity. Analyses of individual emission lines of C VI and O VII permit a more robust measurement of the SWCX contribution and LHB temperature that is less sensitive to inaccuracies in the spectral models for charge exchange. The derived temperatures for the LHB and halo are consistent between high and low latitude observations, and compatible with prior values reported in the literature. Emission around 0.9 keV observed only at low latitudes can be explained by unresolved dM stars.

These results are not presented as a complete description of the sources of the Galactic DXRB. The spectra from these brief sounding rocket observations (which consist of only two pointings with less than 11 minutes of observing time) have relatively poor statistical precision and average over a large solid angle. Thus, a relatively simple model can suffice for these observations—one that neglects complexities that are well-established from other measurements. Examples include the strong case against a single temperature halo from emission-absorption studies (Yao & Wang 2007; Yao et al. 2009), convincing evidence for substantial contributions to 1/4 keV emission at high latitudes from $1.0 \times 10^6 \text{ K}$ emitting regions in a multi-phase halo (e.g., Kuntz & Snowden 2000), and the finding that the hot halo is very non-uniform, with 20% of high-latitude on/off cloud observations showing almost no distant O VII or O VIII emission and generally very different distributions of emissivity in these two lines (Henley & Shelton 2015). Additionally, the models used for SWCX are quite crude in comparison to thermal emission models. Solar wind ion abundances are highly variable and unlikely to correspond to a single temperature as assumed here, and the line emission ratios are derived from models known to be inaccurate by factors of two and more at solar wind velocities.

But there is the promise of major improvements in the near future. We have already used this same XQC payload as a detector on the merged beam collision facility at Oak Ridge National Laboratories to make some preliminary measurements of line ratios from charge exchange as a function of velocity that illustrate limitations of current calculations (Defay et al. 2013; Fogle et al. 2014; Seely et al. 2017). The installation has now been greatly improved and will soon be collecting better data on lines from ion-neutral pairs of astrophysical interest. The eROSITA mission should soon begin a series of eight *ROSAT*-like all-sky surveys with CCD energy resolution. A small orbital mission of an XQC-like instrument could quickly improve on the results presented here by orders of magnitude, and the very high spectral resolution would nicely complement the very high spatial resolution and statistical precision of the eROSITA surveys.

We would like acknowledge the contributions of many graduate and undergraduate students who have contributed to the XQC instrument. We also thank the Luxel Corporation and Kari Kripps for the fabrication of the IR-blocking filters and support meshes. We are grateful for the support of the sounding rocket staff at Wallops Flight Facility and White Sands Missile Range. Finally, we thank the anonymous referee for their careful

reading of the manuscript and helpful comments. The contributions of the Goddard co-authors were supported by the National Aeronautics and Space Administration under an award issued through its Astrophysics Research and Analysis Program. This work was supported in part by NASA grant NNX16AM31G.

ORCID iDs

Dallas Wulf  <https://orcid.org/0000-0001-7314-9496>
 Kelsey M Morgan  <https://orcid.org/0000-0002-6597-1030>
 Dan McCammon  <https://orcid.org/0000-0001-5170-4567>
 Andrew E Szymkowiak  <https://orcid.org/0000-0002-4974-687X>

References

- Anders, E., & Ebihara, M. 1982, *GeCoA*, **46**, 2363
 Anders, E., & Grevesse, N. 1989, *GeCoA*, **53**, 197
 Arnaud, K. A. 1996, in ASP Conf. Ser. 101, *Astronomical Data Analysis Software and Systems V*, ed. G. H. Jacoby & J. Barnes (San Francisco, CA: ASP), 17
 Balucinska-Church, M., & McCammon, D. 1992, *ApJ*, **400**, 699
 Bellm, E. C., & Vaillancourt, J. E. 2005, *ApJ*, **622**, 959
 Bienayme, O., Robin, A. C., & Creze, M. 1987, *A&A*, **180**, 94
 Burrows, D. N., & Mendenhall, J. A. 1991, *Natur*, **351**, 629
 Burrows, D. N., & Mendenhall, J. A. 1993, *AdSpR*, **13**, 83
 Cravens, T. E. 1997, *GeoRL*, **24**, 105
 Crowder, S. G., Barger, K. A., Brandl, D. E., et al. 2012, *ApJ*, **758**, 143
 Das, S., Mathur, S., Nicastro, F., & Krongold, Y. 2019, [arXiv:1907.07176](https://arxiv.org/abs/1907.07176)
 Defay, X., Morgan, K., McCammon, D., et al. 2013, *PhRvA*, **88**, 052702
 Ferrière, K. M. 2001, *RvMP*, **73**, 1031
 Fogle, M., Wulf, D., Morgan, K., et al. 2014, *PhRvA*, **89**, 042705
 Galeazzi, M., Chiao, M., Collier, M. R., et al. 2014, *Natur*, **512**, 171
 Giampapa, M. S., Rosner, R., Kashyap, V., et al. 1996, *ApJ*, **463**, 707
 Greenwood, J. B., Williams, I. D., Smith, S. J., & Chutjian, A. 2001, *PhRvA*, **63**, 062707
 Gupta, A., & Galeazzi, M. 2009, *ApJ*, **702**, 270
 Henley, D. B., & Shelton, R. L. 2015, *ApJ*, **808**, 22
 Koutroumpa, D. 2007, PhD thesis, Pierre and Marie Curie Univ.
 Koutroumpa, D., Lallement, R., Raymond, J. C., & Kharchenko, V. 2009, *ApJ*, **696**, 1517
 Kuntz, K. D., & Snowden, S. L. 2000, *ApJ*, **543**, 195
 Kuntz, K. D., & Snowden, S. L. 2001, *ApJ*, **554**, 684
 Lei, S., Shelton, R. L., & Henley, D. B. 2009, *ApJ*, **699**, 1891
 Liu, W., Chiao, M., Collier, M. R., et al. 2017, *ApJ*, **834**, 33
 Liu, W., Galeazzi, M., & Ursino, E. 2016, *ApJ*, **816**, 82
 Masui, K., Mitsuda, K., Yamasaki, N. Y., et al. 2009, *PASJ*, **61**, S115
 McCammon, D., Almy, R., Apodaca, E., et al. 2002, *ApJ*, **576**, 188
 McCammon, D., Barger, K., Brandl, D. E., et al. 2008, *JLTP*, **151**, 715
 Pearson, K. F. R. S. 1900, *The London, Edinburgh, and Dublin Philosophical Magazine and Journal of Science*, **50**, 157
 Ponti, G., Hofmann, F., Churazov, E., et al. 2019, *Natur*, **567**, 347
 Robertson, I. P., & Cravens, T. E. 2003, *JGRA*, **108**, 8031
 Rosner, R., Avni, Y., Bookbinder, J., et al. 1981, *ApJL*, **249**, L5
 Sanders, W. T., Edgar, R. J., Kraushaar, W. L., McCammon, D., & Morgenthaler, J. P. 2001, *ApJ*, **554**, 694
 Savage, B. D., & Sembach, K. R. 1996, *ARA&A*, **34**, 279
 Schlegel, D. J., Finkbeiner, D. P., & Davis, M. 1998, *ApJ*, **500**, 525
 Scholz, F. W., & Stephens, M. A. 1987, *J. Am. Stat. Assoc.*, **82**, 918
 Seely, D. G., Andrianarijaona, V. M., Wulf, D., et al. 2017, *PhRvA*, **95**, 052704
 Smith, R. K., Bautz, M. W., Edgar, R. J., et al. 2007, *PASJ*, **59**, S141
 Smith, R. K., Brickhouse, N. S., Liedahl, D. A., & Raymond, J. C. 2001, *ApJL*, **556**, L91
 Smith, R. K., Foster, A. R., & Brickhouse, N. S. 2012, *AN*, **333**, 301
 Smith, R. K., Foster, A. R., Edgar, R. J., & Brickhouse, N. S. 2014, *ApJ*, **787**, 77
 Snowden, S. L., Egger, R., Finkbeiner, D. P., Freyberg, M. J., & Plucinsky, P. P. 1998, *ApJ*, **493**, 715
 Snowden, S. L., Egger, R., Freyberg, M. J., et al. 1997, *ApJ*, **485**, 125
 Upreti, Y., Chiao, M., Collier, M. R., et al. 2016, *ApJ*, **829**, 83
 von Steiger, R., Schwadron, N. A., Fisk, L. A., et al. 2000, *JGRA*, **105**, 27217
 Weisskopf, M. C., Guainazzi, M., Jahoda, K., et al. 2010, *ApJ*, **713**, 912
 Wulf, D., Jaeckel, F., McCammon, D., & Morgan, K. M. 2016, *JLTP*, **184**, 431
 Wulf, D., Jaeckel, F., McCammon, D., & Morgan, K. M. 2019, submitted
 Yao, Y., & Wang, Q. D. 2007, *ApJ*, **658**, 1088
 Yao, Y., Wang, Q. D., Hagihara, T., et al. 2009, *ApJ*, **690**, 143
 Yoshino, T., Mitsuda, K., Yamasaki, N. Y., et al. 2009, *PASJ*, **61**, 805